Non-Gaussian Estimation of a Potential Flow by an Actuated Lagrangian Sensor Steered to Separating Boundaries by Augmented Observability

Francis D. Lagor, *Member, IEEE,* Kayo Ide, and Derek A. Paley, *Senior Member, IEEE*

Abstract

This paper presents an architecture for estimation of a flow field using a hypothetical oceanographic vehicle that is guided along paths of high flow-field observability, a concept quantifying the informativeness of a path. Sampling trajectories that pass close to saddle points along separating boundaries of invariant sets provide high observability of flow-field parameters. The estimation and control framework consists of a model predictive controller that utilizes a measure known as the empirical augmented unobservability index to select from candidate trajectories generated by steering the vehicle to separating boundaries of invariant sets. Empirical augmented observability extends empirical observability to account for prior uncertainty when performing path planning based on observability. While following a selected trajectory, the vehicle takes measurements of its position (e.g., GPS measurements) and accounts for its own actuation to produce Lagrangian measurements. The vehicle assimilates this Lagrangian data in a Gaussian Mixture Kalman Filter, which is a nonlinear/non-Gaussian filter, to recursively improve its map of the flow field. Using the posterior uncertainty of the map, the vehicle plans new candidate routes and continues to sample adaptively. The performance of this estimation architecture is demonstrated for a simplified dynamic model of a pair of ocean eddies.

Index Terms

path planning, observability, adaptive sampling, nonlinear filtering, ocean sampling

F. Lagor is with the Department of Mechanical and Aerospace Engineering, University at Buffalo, The State University of New York, Buffalo, NY 14260 USA e-mail: flagor@buffalo.edu.

K. Ide is with the Department of Atmospheric and Oceanic Science, University of Maryland, College Park, MD 20742 USA e-mail: ide@umd.edu.

D. Paley is with the Department of Aerospace Engineering and the Institute for Systems Research, University of Maryland, College Park, MD 20742 USA e-mail: dpaley@umd.edu.

Funding for this work was provided by the National Science Foundation award CMMI1362837.

I. Introduction

Oceanographic forecasters rely on essential data provided by ocean observing systems to infer the approximate state of the oceans. These observing systems consist of ocean sampling vehicles that must provide coverage for vast areas and remain deployed for extended durations. One such example system is Argo [1], a network of approximately 3,750 floats that passively drift in the ocean while collecting hydrographic measurements (e.g., salinity and temperature) during vertical dives. Although Argo measurements are focused on temperature and salinity profiles, researchers have used their position data for examining currents at their operating depth of approximately 1000 m [2], since satellite position fixes of these vehicles also encode flow-current measurements as they drift. Other researchers have considered the potential for ocean observing networks that merge the information from various heterogeneous sensors to estimate ocean currents at the surface [3]. As forecasters rely increasingly on the use of ocean data, these sensor networks must increase in sampling fidelity to adequately capture the dynamic state of the 361,900,000 square kilometers of world oceans [4].

To address the vastness of world oceans, future ocean observing systems should include autonomous vehicles such as ocean gliders (long-endurance vehicles capable of steering and buoyancy-driven propulsion) for adaptive sampling [3], [5], [6]. Autonomous sampling vehicles may reduce oceanographic uncertainty by selecting beneficial routes for collection of measurements in response to uncertainties in estimated environmental processes [7], [8]. Ocean gliders have already proven useful for adaptive sampling in field experiments [9], however more work is necessary to develop an adaptive sampling architecture to use their position data (i.e., Lagrangian data) during extended deployments. Position data contains rich information about the underlying flowfield.

A self-propelled vehicle acts as a quasi-Lagrangian sensor if its position data (e.g., GPS measurements when surfacing) are used as measurements after accounting for the control effort exerted by the vehicle. Planning feasible, efficient, and information-rich routes is essential for long-endurance vehicles like gliders that are minimally actuated. Prior research has planned time-optimal and energy-optimal paths for continuously self-propelled vehicles [10]–[12]. However, there still exists no comprehensive framework for ocean flow estimation from position data that utilizes forecasts of ocean currents for path planning of autonomous vehicles with minimal actuation.

Our estimation and control architecture enables a self-propelled vehicle to estimate unknown parameters of the surrounding flow modeled using potential flow theory. There are three main components of the architecture: (i) the Augmented-Observability Planner with expected cost (A-OP) evaluates multiple possible paths and selects one that maximizes the augmented observability of the flow-field parameters; (ii) a hybrid steering controller that creates candidate vehicle paths by guiding the vehicle along highly observable routes; and (iii) the Gaussian Mixture Kalman Filter (GMKF), which performs nonlinear/non-Gaussian estimation of the states and parameters. The A-OP plans paths that maximize observability of the flow field parameters, given that the vehicle already has some prior knowledge and that the prior probability over the parameter space may be non-Gaussian. The hybrid steering controller ensures convergence of the vehicle to a closed, convex curve (a closed streamline of flow field) in the presence of an underlying flow that causes the vehicle to drift. The GMKF estimator integrates the non-Gaussian uncertainty developed during the propagation of the state through the flow field.

The ability to infer uniquely the parameters or the initial state of a system by analyzing its output collected over specified time interval is the property of observability in dynamical systems theory. Other works (e.g., [13] and [14]) have considered observability or empirical observability (its approximation in the case of a nonlinear system) to plan informative trajectories for sampling vehicles. The trajectories can be considered informative due to the close connection between observability and information theory (e.g., see [15]). Hinson et al. [13] analytically obtain a trajectory that maximizes inertial position and heading observability for a vehicle in a uniform flow. Using linearized dynamics, their optimization is posed to select a path that minimizes the condition number for the linear observability Gramian. Unfortunately, analytical solutions exist only in specialized cases [13]. DeVries et al. [14] confront this difficulty with an optimization evaluated over a finite set of pre-selected candidate trajectories formed through discretization. Leonard et al. [16] launched an adaptive sampling field experiment in Monterey Bay that utilized a similar optimization over a set of multivehicle sampling patterns with respect to a performance metric based on estimation error. Optimization over a finite set of candidate trajectories reduces computational cost and enables incorporation of other control objectives by using them to first generate the candidate trajectories.

Path planning in an uncertain environment requires observability computations that depend on uncertain parameters or states. To include the uncertainty of the state/parameter estimates in observability-based path planning, we introduce the augmented observability Gramian in [17], which is the Hessian matrix of an optimal data assimilation strategy for initial state inference. Augmented observability combines the observability Gramian with the inverse of the state error covariance, which captures the uncertainty present in the estimate of the current state. We demonstrate via numerical experiment in [17] that augmented observability-based path planning based on Gaussian prior knowledge yields the vehicle path with observability that is most complementary to prior information for initial state inference. Augmented observability plays a central role in the path planning portion of the control architecture of this paper. Furthermore, we create the A-OP, which extends augmented observability-based path planning to probability densities functions (PDFs) that may not be Gaussian by representing the uncertainties using a Gaussian mixture model (GMM). The components of the GMM provide weighted realizations from the prior density that can be analyzed individually for augmented observability. We achieve an overall analysis that combines the component analyses by calculating an (approximate) expected cost with weights drawn from the mixture model.

An architecture for control of autonomous oceanographic vehicles and flow estimation using position data should account for barriers to transport formed by coherent flow structures. Coherent structures can form entrained regions of the flow field, also known as (almost) invariant sets; a sampling platform cannot escape an invariant set without expending control effort. Salman et al. [18] address this issue of the influence of flow field geometry on estimation performance by optimizing locations for the launch of unactuated drifting vehicles. We make use of the separating boundaries of invariant sets during path planning; we claim that sampling along these boundaries yields higher observability of the overall flow field. This claim complements the work of Michini et al. [19] in which a three-robot team is constructed to follow coherent structure boundaries for purposes related to energy- and time-optimal transport. The prior works [20], [21] describe coherent-structure path following for surface vessels in laboratory experiments using vehicles that measure local flow velocity. Krener and Ide [22] proposed deployment of Eulerian and Lagrangian sensors in a two-vortex flow according to an empirical observability analysis. We further their findings for Lagrangian measurements by showing that separating boundaries are associated with high observability of a parameterized flow field.

We utilize a two-vortex model for path planning studies to test out our estimation and control framework, because examining the two-vortex model naturally extends prior observability-based path planning work in a two-vortex flow without actuated vehicles [22], in stationary point vortex flow [14] and time-invariant, uniform flow [13]. Point-vortex and potential flow methods have been used to model geophysical flows including ocean eddies in [23] and [24]. Two-vortex or vortex dipole models are relevant to oceanography because coherent vortex dipoles have been observed in the offshore California current [25] and are known to occur regularly where the southward branch of the East Madagascar Current separates from the continental shelf south of Madagascar, where they contribute to mixing processes [26]. The work [27] provides additional details on the modification of potential flow models for increasing physical relevancy to include rotational effects (in quasigeostrophic balance between the pressure gradient and Coriolis acceleration component), changes in vortex circulation strength in time, and the formation and shedding of vorticity in time. The two-vortex model is useful in path-planning studies due to the model's analytical representation and the presence of coherent structures, which act as barriers to transport. For general ocean data, a technique for identifying coherent flow structures is Finite-Time Lyapunov Exponent (FTLE) analysis [20].

Steering a vehicle along separating boundaries of invariant sets requires a control law for path following. Zhang and Leonard [28] developed such a control law but did not include the effects of the flow field on the vehicle. We propose a hybrid controller for a vehicle modeled as a self-propelled particle that includes a streamline control law and a streamfunction-value control law. Under this hybrid controller, the vehicle navigates along the separating boundaries of a spatially nonuniform, time-invariant flow field, while periodically re-assessing its chosen route. The streamline controller is a novel combination of an existing steering algorithm in the absence of flow [28] with an existing transformation of the vehicle speed and flow-relative heading [29] for a steering controller in a time-invariant flow field. This control law guarantees that the vehicle steers to a unique closed streamline of the flow by constructing a Bertrand family of curves from the target streamline, which must be a closed, regular, simple curve. We further construct a valid region for the streamline control law by showing that within this region, a unique closest point exists on the streamline, thereby extending the existing controller of [28] to closed streamlines that are nonconvex. The streamfunction-value control law steers the vehicle to the region of validity of the streamline control law. Taken together, these control laws are a hybrid control approach that generates candidate trajectories along highly observable paths, i.e., the separating boundaries of invariant sets.

Another essential element in the adaptive sampling architecture is a state estimator for non-Gaussian densities and nonlinear dynamics, the Gaussian Mixture Kalman Filter (GMKF). The GMKF replaces non-Gaussian PDFs with approximations based on a mixture of Gaussians, a technique that has been shown to be highly effective for nonlinear filtering [30]. Following [31], we choose the number of Gaussians in the approximation to provide the simplest fit (i.e., using the fewest parameters) of a Gaussian mixture to the data through minimization of the Bayesian Information Criterion (BIC). These elements combine to form a novel architecture for estimation of an unknown flow field using measurements of vehicle position. The primary novelty in this framework lies in the use of the GMKF estimator to inform the A-OP planner, by which the A-OP weighs candidate paths with respect to how their anticipated observability gains complement prior information. Candidate trajectories are generated by the hybrid controller steering along paths of high observability for multiple flow-field realizations, based on a non-Gaussian prior density over the flow-field parameters. The A-OP evaluates the pre-selected control signals for the most informative path through an analysis of augmented observability. The GMKF processes the Lagrangian data (after subtracting the vehicle's control actions) to output updated estimates of the flow-field parameters.

This paper contributes: (i) a hybrid control law for steering self-propelled vehicles along separating boundaries of invariant sets in a time-invariant flow field; (ii) a novel method of scoring candidate trajectories by calculating the approximate expected cost of the augmented unobservability index; and (iii) a guided-Lagrangian adaptive sampling architecture for estimation of flow-field parameters. Numerical experiments that demonstrate the additional benefits of each element in the proposed architecture are presented for a single vehicle navigating in and estimating the strengths and locations of a pair of ocean eddies modeled as two co-rotating, potential-flow vortices.

The paper represents an integration and significant extension of the conference proceedings [32], [33]. The work [33] demonstrates that a kinematically controlled, infrequently actuated vehicle can obtain greater flow-field observability than a passively drifting vehicle by executing a user-defined tour of separating boundaries of invariant sets. The work [32] shows that a dynamic, steering controlled vehicle can achieve improved estimation performance compared to a drifting vehicle by using the GMKF while steering along boundaries prescribed in a user-defined tour. This paper proposes path planning for navigation along invariant-set boundaries without requiring a user-specified tour; the vehicle considers candidate trajectories guided to all reachable invariant-set boundaries and selects the control that minimizes the expected cost of augmented unobservability of flow-field parameters. This paper also utilizes the concept of augmented observability from [17] to perform closed-loop flow-field navigation and estimation of an entire flow field by a guided Lagrangian sensor using feedback and augmented observability analysis. In contrast to [32], which uses only the mean state estimate from the GMKF, the planning algorithm in this work utilizes the entire posterior probability density by taking multiple samples of the system parameters for generation of the candidate trajectories.

Section II presents background material needed for the remainder of the paper, including a description of the two-vortex system, steering control law, observability-based path planning, and GMKF. Section III motivates and develops a controller for steering to the boundaries of invariant sets. Section IV presents the comprehensive framework for flow-field estimation using an guided Lagrangian sensor. Section V presents numerical experiments demonstrating the sampling framework. Section VI concludes the paper and suggests extensions to this work.

II. Background

A. Two-vortex model

A pair of ocean eddies may be represented by an idealized model consisting of two point vortices. A time-invariant, incompressible flow $f \in \mathbb{C}$ evaluated at $z \in \mathbb{C}$ may be represented using the gradient of a streamfunction $\psi = \psi\left(z, \overline{z}\right)$ such that

$$f = -2i\frac{\partial \psi}{\partial \overline{z}}, \tag{1}$$

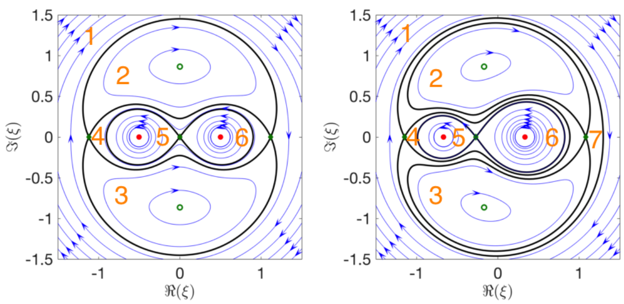

(a) $\Gamma_2 = \Gamma_1$ (b) $\Gamma_2 = 2\Gamma_1$

Fig. 1. a), b) Co-rotating frame streamlines and fixed points for the two-vortex system [17]

where the overline operator denotes complex conjugation and the conjugate complex partial derivative operator is given by $\partial/\partial\overline{z} = \frac{1}{2}\left(\partial/\partial x + i\partial/\partial y\right)$ [35]. The flow field associated with two point vortices located at z_1 and z_2 in $\mathbb{C}$, with circulation strengths Γ_1 and Γ_2, respectfully, has the streamfunction

$$\psi\left(z,\overline{z}\right) = -\frac{1}{2\pi}\left(\Gamma_1 \log|z - z_1| + \Gamma_2 \log|z - z_2|\right). \tag{2}$$

For each vortex, flow from the opposing vortex generates the dynamic motion

$$\dot{z}_j = -\frac{i\Gamma_q}{2\pi}\frac{z_j - z_q}{|z_j - z_q|^2}, \tag{3}$$

for $j, q = 1, 2$ and $j \neq q$. Vortices that have circulation strengths with the same sign orbit around a fixed center of vorticity $z_{\text{cv}} = \left(\Gamma_1 z_1 + \Gamma_2 z_2\right)/\left(\Gamma_1 + \Gamma_2\right)$ with an angular rate $\omega = \left(\Gamma_1 + \Gamma_2\right)/\left(2\pi|z_1 - z_2|^2\right)$. The mapping

$$z = \xi e^{i(\omega t + \phi)} + z_{\text{cv}} \tag{4}$$

transforms between a reference frame centered at z_{cv} rotating with the vortex pair and a fixed inertial frame, where ϕ is a phase angle from the vortex pair's initial orientation and $\xi \in \mathbb{C}$ is the location in the co-rotating frame. In the co-rotating frame, the streamfunction that corresponds to the co-rotating flow f_R under relationship (1) is

$$\psi_R\left(\xi,\overline{\xi}\right) = -\frac{1}{2\pi}\left(\Gamma_1 \log|\xi - \xi_1| + \Gamma_2 \log|\xi - \xi_2|\right) + \frac{\omega}{2}|\xi|^2, \tag{5}$$

where ξ_1 and ξ_2 correspond with the z_1 and z_2 vortex locations, respectively [32].

Figure 1a presents the streamlines in the co-rotating frame for two vortices of equal strength. Five fixed points of the flow field are shown: two centers are shown as circles and three saddles appear as diamonds. There are six invariant sets; the black lines represent their boundaries. These boundaries, or separatrices, are the unstable and stable manifolds associated with the saddle fixed points that they intersect. Figure 1b shows seven invariant sets are induced for two vortices of unequal strengths $\Gamma_1 > \Gamma_2 > 0$.

B. *Steering navigation of a self-propelled vehicle*

A model for a self-propelled vehicle with speed ρ in the complex plane $\mathbb{C}$ without a flow field present is [36]

$$\dot{z} = \rho e^{i\beta} \quad \text{with} \quad \dot{\beta} = v, \tag{6}$$

where v is an input for the vehicle turning rate. This model is commonly used for path-planning of autonomous vehicles that self-propel with a nominal speed ρ and have steering as their primary means of control.

Consider a mobile sensor with speed α advected by an underlying flow field f. The model (6) may be modified to additively include the flow velocity such that

$$\dot{z} = \alpha e^{i\theta} + f \quad \text{with} \quad \dot{\theta} = u, \tag{7}$$

where θ measures the counterclockwise angle of the direction of self propulsion, and u is the steering input [29].

To compensate for the influence of the flow field during control design, Paley and Peterson [29] define the speed ρ in (6) to be the total vehicle speed $\rho = |\alpha e^{i\theta} + f|$. They define the heading β in (6) to be the angle $\beta = \arg(\alpha e^{i\theta} + f)$ of the total velocity vector. Under these transformations, the model with flow (7) simplifies to the model without flow (6). The inputs of (7) and (6) are related by [29]

$$u = \frac{v - \left\langle \dot{f}, ie^{i\beta} \right\rangle}{1 - \rho^{-1} \left\langle f, e^{i\beta} \right\rangle}. \tag{8}$$

Observe that if the vehicle cannot make forward progress, that is, if $\left\langle f, e^{i\beta} \right\rangle = \rho$, then (8) becomes singular [29]. One approach to address this issue in strong flows is to use a saturation function on the steering input [36]. Transformation (8) enables the use of a control developed by Zhang and Leonard [45] for a self-propelled vehicle without a flow field present.

Zhang and Leonard [45] use a path frame to navigate a (possibly non-constant speed) vehicle through a scalar field $\Theta(z)$ to a level-set $\{z : \Theta(z) = \Theta^{\text{des}}\}$ for the desired value Θ^{des}. Let $a_1 = e^{i\beta}$ represent the direction of a vehicle's instantaneous velocity. Form $a_2 = ia_1$, so that $a_1, a_2 \in \mathbb{C}$ define a path frame for the trajectory of the vehicle. The path frame evolves in time according to the dynamics [45]

$$\dot{a}_1 = va_2 \quad \text{and} \quad \dot{a}_2 = -va_1. \tag{9}$$

The solutions of (6) and (9) provide trajectories for the vehicle and its path frame.

Let path frame (a_1, a_2) be co-located at z with the vehicle, and build an additional reference frame (b_1, b_2) that is also located at z with b_2 aligned in the direction of the gradient of the field, where b_1 resulting from a clockwise rotation of b_2, i.e.,

$$b_2 = \frac{\frac{\partial \Theta}{\partial \bar{z}}}{\left|\frac{\partial \Theta}{\partial \bar{z}}\right|} \quad \text{and} \quad b_1 = -ib_2. \tag{10}$$

Figure 2a shows these definitions, using $\Im(\cdot)$ and $\Re(\cdot)$ to denote the imaginary and real operators, respectively. Take η to be the angle from a_1 to b_1. Zhang and Leonard [45] consider how η and Θ change while the vehicle moves through the scalar field in order to formulate Proposition 1.

Proposition 1 (Zhang and Leonard [45])**.** *Consider a scalar field $\Theta(z)$ over a connected subset of $\mathbb{C}$. Represent the extrema of $\Theta(z)$ by $-\infty \leq \Theta_{min} < \Theta_{max} \leq \infty$. Further, assume $|\partial\Theta/\partial\bar{z}| < \infty$ and $|\partial^2\Theta/\partial z\partial\bar{z} + \partial^2\Theta/\partial\bar{z}^2| < \infty$. Allow $|\partial\Theta/\partial\bar{z}| = 0$ only at finitely many points where $\Theta(z)$ attains the value of either Θ_{min} or Θ_{max}. Let $\Pi(\Theta)$*

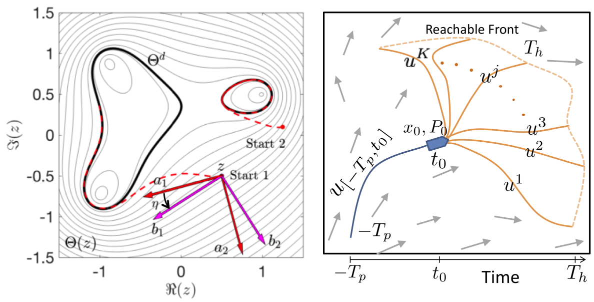

(a) (b)

Fig. 2. a) Notation used for steering to a desired, scalar level set. b) Observability-based path planning [17]

be a scalar function (see the technical requirements in the Supplemental Materials document). Assume the initial condition is such that $\eta(t_0) \neq \pi$ *and* $|\partial\Theta/\partial\bar{z}| \neq 0$. *Then, the control law*

$$v = \rho\left(\kappa_a \cos\eta + \kappa_b \sin\eta - 4\frac{d\Pi}{d\Theta}\bigg|_{\Theta(z)}\left|\frac{\partial\Theta}{\partial\bar{z}}\right|\cos^2\frac{\eta}{2} + K_1\sin\frac{\eta}{2}\right), \tag{11}$$

with

$$\kappa_a = \frac{-1}{|\frac{\partial\Theta}{\partial\bar{z}}|}\left\langle b_1, \frac{\partial^2\Theta}{\partial z\partial\bar{z}}b_1 + \frac{\partial^2\Theta}{\partial\bar{z}^2}\bar{b}_1\right\rangle$$

and

$$\kappa_b = \frac{1}{|\frac{\partial\Theta}{\partial\bar{z}}|}\left\langle b_1, \frac{\partial^2\Theta}{\partial z\partial\bar{z}}b_2 + \frac{\partial^2\Theta}{\partial\bar{z}^2}\bar{b}_2\right\rangle,$$

guides a steered, self-propelled vehicle so that as $t \to \infty$, $\eta \to 0$ *and* $\Theta \to \Theta^{des}$.

Figure 2a presents two simulations of a vehicle guided by control law (11) for different initial conditions and the same desired value Θ^{des}, showing that the final curve is dependent on the initial condition. Section III-D makes use of this proposition to form two new control laws: the first control law steers the vehicle to a unique, closed streamline, and the second control law steers the vehicle so that it enters the applicable range of the first controller. We combine these control laws to create a hybrid controller used in our adaptive sampling architecture. The hybrid steering controller guides the vehicle to coherent structures that appear in the co-rotating frame of the two-vortex system. The control that is desired in the co-rotating frame is converted back to the inertial frame for simulation.

C. Augmented observability-based path planning

Observability-based path planning is a model-predictive control technique of forecasting the anticipated system outputs given a finite set of K control inputs $\{u_j\}_{j=1}^{K}$ and assessing the system observability along the system trajectory for each candidate control signal. Using a scalar measure of observability, such as the unobservability index [22], the control choices may be compared and optimized over a finite set of control parameters. This model-predictive control strategy assumes that the candidate control signals are generated by another means, e.g., according to a secondary control policy. Figure 2b depicts this process for a vehicle at time t_0 assessing control signals over the planning interval $[t_0, T_p]$.

From linear systems theory, if the observability Gramian is full rank, then the initial state of the system can be inferred from measurements, and the system is observable. Krener and Ide [22] constructed an empirical observability Gramian that applies to nonlinear systems and also gives a measure of the degree of observability through the unobservability index. Consider the nonlinear system,

$$\begin{aligned} \dot{x}(t) &= g(t, x(t)) \\ y(t) &= h(t, x(t)) + \mu(t), \end{aligned} \tag{12}$$

where $x \in \mathbb{R}^n$, $y \in \mathbb{R}^p$, f and h are known, nonlinear functions, and measurement noise $\mu(t)$ is a white Gaussian stochastic process with covariance $R(t)$. For the two-vortex problem considered in this paper, the state vector is

$$x = (\Gamma_1, \Re(z_1), \Im(z_1), \Gamma_2, \Re(z_2), \Im(z_2), \Re(z), \Im(z))^T , \tag{13}$$

where z denotes the location of the sampling vehicle.

Let $\phi(\cdot, t_0, x(t_0))$ denote the state solution to (12) from $x(t_0)$ at t_0. Consider the $2n$ perturbed initial conditions $x^{\pm j}(t_0) = x(t_0) \pm \epsilon e_j$, for $j = 1, \ldots, n$ where $\epsilon > 0$, is the perturbation size, e_j is the unit vector with 1 in the jth location and zeros elsewhere, and annotate the corresponding state solution $\phi^{\pm j}$ similarly. The empirical observability Gramian is

$$\mathcal{W}_{\text{eo}}(t_0, t, x(t_0)) = \int_{t_0}^{t} \Psi_e^T R(\tau)^{-1} \Psi_e d\tau, \tag{14}$$

where $\Psi_e = \Psi_e(\tau, t_0, x(t_0))$ is an $n \times n$ matrix with jth column specified by

$$[\Psi_{\text{e}}(\tau, t_0, x(t_0))]_j = \frac{h(\tau, \phi^{+j}) - h(\tau, \phi^{-j})}{2\epsilon}, \tag{15}$$

where $\phi^{\pm j} = \phi^{\pm j}(\tau, t_0, x(t_0))$. Note that Ψ_e is an approximation to $\partial h / \partial x_0$ [17], [22]. For a linear system, as $\epsilon \to 0$ with $R(\tau) = \mathbb{I}$, $\mathcal{W}_{\text{eo}}$ reduces to the usual linear observability Gramian [22], [37].

One can assess the degree of observability by considering the minimum eigenvalue of the empirical observability Gramian, which is zero if $\mathcal{W}_{\text{eo}}$ is singular and nonzero when the initial state is observable. The unobservability index is [22]

$$\nu(\mathcal{W}_{\text{eo}}) = \frac{1}{\lambda_{\text{min}}(\mathcal{W}_{\text{eo}})}. \tag{16}$$

When ν is small, observability is high. The index ν measures the difficulty of initial-condition inference for the nonlinear system over the interval $[t_0, t]$.

Consider now the case in which we have prior background information regarding the initial state $x(t_0)$. Specifically, assume the uncertainty of the initial condition (prior to observing the output) is Gaussian distributed about a mean vector x_0 with covariance P_0, such that $x(t_0) \sim \mathcal{N}(x_0, P_0)$. In [17], we derive an observability Gramian that is augmented with information contained in P_0^{-1} by using an optimal data assimilation strategy known as 4D-Var. We extend augmented observability to the nonlinear setting for system (12) by utilizing the empirical observability Gramian of Krener and Ide [22], yielding the empirical augmented observability Gramian

$$\mathcal{W}_{\text{ea}}(t_0, t, x(t_0)) = \int_{t_0}^{t} \Psi_e^T R(\tau)^{-1} \Psi_e d\tau + P_0^{-1}. \tag{17}$$

We also define the augmented unobservability index

$$\nu_a(\mathcal{W}_{ea}) = \frac{1}{\lambda_{\min}(\mathcal{W}_{ea})} = \frac{1}{\lambda_{\min}\left(\mathcal{W}_{eo} + P_0^{-1}\right)}, \tag{18}$$

which quantifies how difficult initial-condition inference is given the anticipated system measurements and the prior information and will serve as a cost to minimize during path planning.

D. Gaussian Mixture Kalman Filter

The Lagrangian sampling framework developed in this paper performs state estimation using a Gaussian Mixture Kalman Filter (GMKF). The GMKF performs nonlinear propagation of uncertainty in the state and permits non-Gaussian PDFs that often arise in Lagrangian data assimilation in nonlinear flow fields. Filters based on Gaussian mixture models (GMMs) have appeared previously in various forms (e.g., [38], [39], or [31]). The GMKF filter in this paper is based on the GMM-DO filter of [31] which combines GMMs and dynamically orthogonal field equations (DO). The GMM-DO filter is unique because it implements automated selection of the GMM complexity (i.e. the number of Gaussians to use in the GMM). Here, we utilize the GMM-DO filter, without the DO equations—instead we directly propagate the estimate of the state.

Assume a probability density function that can be represented using M multivariate Gaussians. Each Gaussian $\mathcal{N}(x; \overline{x}_m, P_m)$ has mean vector $\overline{x}_m$ and covariance matrix P_m, for $m = 1, \ldots, M$, as well as a scalar weight w_m. To be a valid PDF, the scalar weights of all M Gaussians must sum to unity (i.e., $\sum_{m=1}^{M} w_m = 1$). The GMM [31]

$$p\left(x; \{(w_m, \overline{x}_m, P_m)\}_{m=1}^{M}\right) = \sum_{m=1}^{M} w_m \mathcal{N}(x; \overline{x}_m, P_m) \tag{19}$$

is a weighted sum of the M component Gaussians. Equation (19) is capable of modeling highly non-Gaussian densities depending on the choices of means, covariances, weights, and number of components.

The GMKF is summarized in Algorithm 1. The GMKF samples an ensemble of realizations from the prior probability density of state. After sampling, the GMKF forecasts each ensemble member according to the nonlinear dynamics. Then, the GMKF creates a best-fit approximation to the ensemble using a mixture of Gaussians of specified complexity through an Expectation-Maximization (EM) algorithm that automatically selects the means, covariances, and weights [40]. For a GMM of given complexity, the GMKF of [31] evaluates the Bayesian Information Criterion (BIC)

$$\text{BIC} = -2\sum_{j=1}^{N} \log p(x_j | \Omega_{\text{EM}}; M) + K \log N, \tag{20}$$

where N is the number of ensemble members, K is the number of model parameters, and Ω_{EM} represents the set of parameters found by the EM algorithm (i.e., means, weights, and covariances). Observe that the BIC has a goodness-of-fit term and a term that penalizes model complexity [31]. The GMKF of [31] evaluates GMMs of increasing complexity so that a local minimum in the BIC score may be identified. We seek the mixture model that best fits the ensemble data; the model-complexity penalty in the BIC encourages a simple model to be preferred [31]. After fitting a GMM to the ensemble spread, the next filtering step is the assimilation of observations.

Input: GMM for prior PDF

Output: GMM for analysis PDF

Parameters: N, `maxComplexity`, and covariance matrices Q, R

1: Sample N ensemble members from the prior PDF.
2: Integrate the ensemble in time with process noise taken from $\mathcal{N}(0,(t_k - t_{k-1})Q)$
3: Fit a GMM to the forecast ensemble using the EM algorithm with $M = 1$. Evaluate the BIC.
4: **for** $m = 2$ to `maxComplexity` **do**
5: Fit m Gaussians in GMM and evaluate the BIC.
6: If the BIC increases, stop and set $M = m - 1$.
7: **end for**
8: Update the weight for each Gaussian in the GMM:

$$w_m^a = \frac{w_m^f \mathcal{N}(y; H\overline{x}_m^f, HP_m^f H^T + R)}{\sum_{q=1}^M w_q^f \mathcal{N}(y; H\overline{x}_q^f, HP_q^f H^T + R)}$$

9: Find the Kalman gain, analysis mean, and analysis covariance for each Gaussian:

$$K_m = P_m^f H^T \left(HP_m^f H^T + R\right)^{-1}$$
$$\overline{x}_m^a = \overline{x}_m^f + K_m(y - H\overline{x}_m^f)$$
$$P_m^a = (I - K_m H)P_m^f$$

Algo. 1. The Gaussian Mixture Kalman Filter (GMKF) [31]

For Lagrangian observations, replace the nonlinear operator h in (12) with the matrix H that acts linearly to pull out the vehicle position information, i.e.,

$$y(t_k) = Hx(t_k) + \mu(t_k) \quad \text{with} \quad \mu(t_k) \sim \mathcal{N}\left(0, R(t_k)\right). \tag{21}$$

Assimilation of the measurement occurs according to a Kalman filter update equations that are modified to include weight updates for the GMM components as well. Steps 8 and 9 in Algorithm 1 are derived in [31] and correspond to direct application of Bayes' rule under the assumption that the forecast PDF is a GMM. Step 8 sequentially evaluates the likelihood $\mathcal{N}(y; H\overline{x}_m^f, HP_m^f H^T + R)$ that the measurement is a realization from each forecasted, component Gaussian (i.e., Gaussian m is evaluated using its forecast mean $\overline{x}_m^f$ and covariance P_m^f) and uses it to compute an updated weight for each Gaussian component; the weight update is necessary to ensure that the posterior density is a valid PDF (i.e., the updated weights of the GMM sum to unity). For each mth Gaussian, Step 9 calculates the Kalman gain, updated mean, and updated covariance, respectively. Note that the calculations in Step 9 are the standard Kalman filter update equations applied to Gaussian m. For a complexity of $M = 1$, note that the GMKF reduces to an Ensemble Kalman Filter (EnKF) in which Gaussianity is enforced during assimilation. After assimilation, the posterior PDF becomes the prior PDF and the filtering cycle repeats.

After assimilation of the observation, the posterior PDF that results from the GMKF is a GMM. To extract usable estimates from the GMM of the state, one may implement a mode-finding algorithm (e.g., see [41]) or one may find the mean for the overall distribution. Representing a possibly multimodal PDF with a single mean estimate does not fully make use of the PDF. Section IV designs a path planning algorithm that utilizes the entire posterior PDF by considering multiple components in the GMM, and Section V compares the multi-component path planner

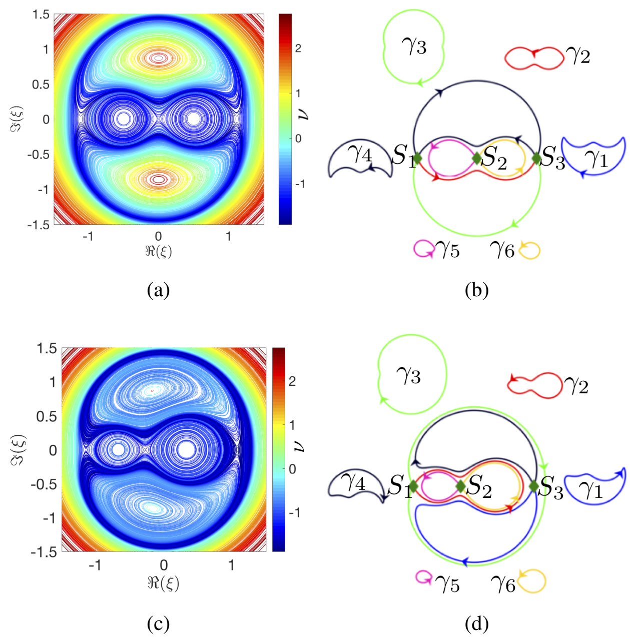

Fig. 3. The unobservability index plotted on a log10 color scale for orbits in the two-vortex system for a) $\Gamma_2 = \Gamma_1$, and c) $\Gamma_2 = 2\Gamma_1$. Extraction of closed, smooth curves for b) $\Gamma_2 = \Gamma_1$, and d) $\Gamma_2 = 2\Gamma_1$; extracted curves are scaled in size.

to one that uses only the mean and covariance of the GMM.

III. Exploration of invariant-set boundaries

This section steers a vehicle along the highly observable separating boundaries of invariant sets, found by extending the stable and unstable manifolds from saddle fixed points of the flow field.

A. *Empirical observability of invariant-set boundaries*

For minimally or infrequently actuated vehicles, it is helpful to understand the natural orbits of the flow field. For one period of rotation of the vortex pair in the two-vortex problem, Krener and Ide [22] calculated the empirical unobservability index to determine locations to launch drifting sensors. We note that the period of rotation for the vortex pair may be shorter or longer than the period of other closed drifter orbits in the two-vortex system. We therefore further the analysis of [22] to full orbits for drifting vehicles as follows. We compute the unobservability index on a grid, similar to [22], but we assume a time horizon that is longer than all closed drifter orbits in the desired domain. Each drifter floats for at least one of period on their individual orbits. For each orbit, we assign the average value of the grid-based unobservability indices for the grid cells that the orbit intersects. Grid-based unobservability analysis can provide an idea of the most informative location for launch for a given time horizon, however unobservability averaged along orbits removes the effect of initial conditions, since different launch locations on the same orbit possess slightly different unobservability indices. Figures 3a and 3c respectively show these calculations for equal- and unequal-strength vortices, based on 1000 orbits from arbitrary initial locations chosen uniformly over the domain and integrated forward in time until $t = 24\pi$. The highest unobservability, corresponding to the least informative orbits, appears near the center fixed points (within regions 2 and 3 as labeled in Figs. 1a and 1b). The lowest unobservability, corresponding to the most informative orbits, appears near the separatrices that divide invariant sets. The separatrices are highly observable because saddle points in a divergence-free flow field eventually divide drifters floating on nearby orbits. These findings provide motivation to sample along highly informative separatrices when taking Lagrangian measurements.

B. Construction of steering targets from separatrices

The following procedure constructs the separatrix geometry for exploration in Lagrangian sampling: (i) locate fixed points of the flow field; (ii) numerically integrate forward in time from each saddle point along the unstable manifolds and along the stable manifolds backwards in time until closely approaching another saddle point or leaving the domain; (iv) remove any redundant curves generated in this process; and (v) build a graph data structure containing saddle points as graph vertices and separating curves as directed graph edges. The resulting graph holds information on the geometry of the flow field, with the coordinates of saddle points, coordinates of points making up separating curves, and the details of connections between saddles and separatrices. Figure 3b presents the resulting saddle graph for a two equal-strength vortex case. The graph consists of three saddle points as vertices, four heteroclinic separatrices (i.e., connections between two distinct saddle points), and two homoclinic separatrices (i.e., connections that start and finish at the same saddle). For the case of two unequal-strength vortices, Fig. 3d provides another example of a saddle graph. In this case, the graph contains three isolated saddles with homoclinic separatrices forming self-loops at each vertex.

The next section presents a hybrid controller for navigation along separating boundaries of invariant sets. The hybrid controller takes in curves meeting certain acceptability criteria (i.e., they are closed, simple, and regular curves) as input to serve as steering targets. Closed curves can be found from separatrices by enumerating all elementary cycles in the saddle graph. We note that path planning over graph structures has previously been explored in the literature (e.g., see [42], [43]). We implement the algorithm of Hawick and James [44] for finding all elementary cycles in the saddle graph. The data structure used in [44] to define the graph allows for multiple edges between vertices and self edges, which are necessary features for saddle graphs of divergence-free flows. The algorithm of [44] generates sequences of vertex identifiers that make up elementary cycles. We assign a separatrix object to each pair of vertices, thereby generating closed, simple curves. We ensure the curves are regular for the steering controller by smoothing the cusps at saddle locations using fourth-order Bézier curves. The saddle graphs in Figs. 3b and 3d are each surrounded by scaled versions of the closed, simple, regular steering targets that result. (See Section SM3 of the Supplemental Materials document for implementation details.)

C. Steering along a unique streamline of the flow

This section presents a steering controller for driving to a closed streamline of the flow by combining the steering controller of [45], which applies to a vehicle without flow, and the flow-relative transformation of [29] to account for flow. Additionally, an existing technique [46] is used to build a Bertrand family of curves around a regular, closed curve to ensure that the vehicle drives to a unique, closed curve. By synthesizing these three existing results, we create a novel steering controller that guides a self-propelled vehicle to a unique, regular, closed streamline of the flow field. Moreover, we specify the region of validity for the controller, in which convergence to a unique streamline is guaranteed.

Recall the dynamics (7) for planning the path of a self-propelled vehicle in a time-invariant flow. Assume that transformation (8) for control u is valid, so that the dynamics may be viewed as model (6). Assume a steering target γ_0 that is a closed, simple, regular[1] curve, possibly enclosing a nonconvex region of the domain. Assign a value of $\chi \in \{-1, +1\}$ to γ_0 for clockwise or counterclockwise orientation, respectively.

Converging to a target curve γ_0 is achieved by building a scalar orbit function $\Phi(z)$ that has γ_0 as a level curve (i.e., for increasing arc length, $\Phi(\gamma_0(s))$ remains constant). Define $(\cdot)'$ as differentiation with respect to arc length s. If curve γ_0 is nonconvex, but closed, simple, and regular, then it belongs to a Bertrand family of curves γ_λ, governed by scalar parameter λ, and an orbit function Φ may be built according to [28], i.e.,

$$\gamma_\lambda(s) = \gamma_0(s) + \lambda i \gamma_0'(s). \tag{22}$$

Additional members of the Bertrand family are formed according to (22) by moving λ in the $i\gamma_0'(s)$ direction, perpendicular to the curve γ_0. A natural orbit function may then be specified as $\Phi(z) = \lambda$ if z lies on the curve γ_λ [28]. Note that the arc length s should be measured along the reference curve γ_0 [28].

For navigation in a flow field described by streamfunction ψ, we require γ_0 to be a closed streamline of the flow that may be found using the Fundamental Theorem of Calculus to be

$$\gamma_0(t) = z(0) + \int_0^t -2i \frac{\partial \psi}{\partial \overline{z}}\Big|_{z(\tau)} d\tau, \quad \text{for} \quad 0 \le t \le T, \tag{23}$$

where $z(0)$ is an initial point on the orbit and T is the period. For the two-vortex problem studied in Section V, ψ is replaced with ψ_R, the streamfunction in the co-rotating frame. The arc length in (22) is given by $s(t) = \int_0^t |-2i\partial\psi/\partial\overline{z}|_{z(\tau)}| d\tau$. To steer a self-propelled particle to the unique orbit γ_0, we construct a Bertrand family of curves γ_λ with orbit function $\Phi(z) = \lambda$ that vanishes when the vehicle lies on γ_0.

Let z_c be the point nearest z that lies on γ_0. We can write $\Phi(z)$ using (22),

$$\Phi(z) = \langle z - z_c, b_2 \rangle . \tag{24}$$

The gradient of the orbit function $\partial\Phi/\partial\overline{z}$ in a Bertrand family of curves is perpendicular to each Bertrand curve. Differentiation of the orbit function in (24) gives

$$\frac{\partial \Phi}{\partial \overline{z}} = \frac{\partial}{\partial \overline{z}} \left(\frac{(z - z_0)\overline{b}_2 - (\overline{z} - \overline{z_0})b_2}{2} \right) = \frac{b_2}{2}, \tag{25}$$

which reveals that the b_2 direction for a vehicle steering in a scalar field (see Section II-B) is also perpendicular to each curve in the family. Since γ_0 is a streamline of the flow, the direction b_2 can also be expressed using the

[1]Closed curves formed from separatrices in a divergence-free flow do not meet the regularity condition at saddle points. However, smoothing using Bézier curves (see SM3) produces boundary curves that avoid saddles and meet the regularity condition.

derivative of the streamfunction ψ evaluated at z_c, such that $b_2 = (\partial\psi/\partial\bar{z}/|\partial\psi/\partial\bar{z}|)\,|_{z_c}$. According to (25), we find the derivatives of Φ necessary for implementation of control law (11) in terms of the ψ to be

$$\frac{\partial^2\Phi}{\partial z\partial\bar{z}} = \frac{1}{2\left|\frac{\partial\psi}{\partial\bar{z}}\right|}\left(\frac{\partial^2\psi}{\partial z\partial\bar{z}} - \frac{\partial^2\psi}{\partial z^2}b_2^2\right),$$

and

$$\frac{\partial^2\Phi}{\partial\bar{z}^2} = \frac{1}{2\left|\frac{\partial\psi}{\partial\bar{z}}\right|}\left(\frac{\partial^2\psi}{\partial\bar{z}^2} - \frac{\partial^2\psi}{\partial z\partial\bar{z}}b_2^2\right).$$

These equations are evaluated at the point z_c, which is the closest point on the reference orbit to the vehicle location z.

The above development of a streamline steering controller assumes that a unique closest point z_c on the reference curve γ_0 exists. However, this condition may not hold for an arbitrary location z near a nonconvex curve. To address possible non-uniqueness, we use the signed curvature κ_s of curve γ_0 to define a region surrounding γ_0 in which the existence of a unique closest point is guaranteed. The signed curvature κ_s from differential curve theory is defined at arc length s according to

$$\gamma''(s) = \kappa_s(s)i\gamma'(s), \tag{26}$$

where $\gamma'(s)$ is the tangent direction and $i\gamma'(s)$ is the normal direction [47]. Equation (26) may also be written to solve for signed curvature, such that $\kappa_s(s) = \langle i\gamma'(s), \gamma''(s)\rangle$. The following proposition defines the region of validity Ω for the streamline steering controller, based on the signed curvature κ_s.

Proposition 2. *Let γ_0 be a twice-differentiable, closed, simple and regular curve in the plane. Let γ_E and γ_I, respectively, represent exterior and interior Bertrand curves defined by offsets*

$$\lambda_E = \frac{\chi}{\min(0, \inf\limits_{\sigma}(\kappa_s(\sigma)\chi))}, \quad \textit{and} \quad \lambda_I = \frac{\chi}{\sup\limits_{\sigma}(\kappa_s(\sigma)\chi)}. \tag{27}$$

Define Ω to be the domain bounded by γ_E and γ_I. If γ_E and γ_I are simple, closed curves,[2] then for each $z \in \Omega$, there exists a unique, closest point z_c on the curve γ_0, in the sense of the Euclidean distance.

Proof. We prove Proposition 2 for a point z that falls between curves γ_0 and γ_I; identically structured arguments hold for points between γ_E and γ_0. Let z_c be the point on γ_0 at arc length s_c that minimizes the Euclidean distance $|z - \gamma_0(s)|$. We will show that z_c exists and is unique. If so, the necessary and sufficient conditions to locally minimize the Euclidean distance $|z - \gamma_0(s)|$, i.e.,

$$\langle\gamma_0'(s_c), z - z_c\rangle = 0, \tag{28}$$

$$\langle\gamma_0''(s_c), z - z_c\rangle < 1, \tag{29}$$

must be satisfied. Since $|\lambda_I| > 0$ and γ_I is simple by assumption, γ_I cannot cross γ_0 and it does not have self-intersections. Since $|\lambda_I| \geq 0$, for every z between γ_0 and γ_I, there exists a λ and an arc length s_c, such that

[2]Note that for the special case of curve γ_0 enclosing a convex region, γ_E lies at infinity.

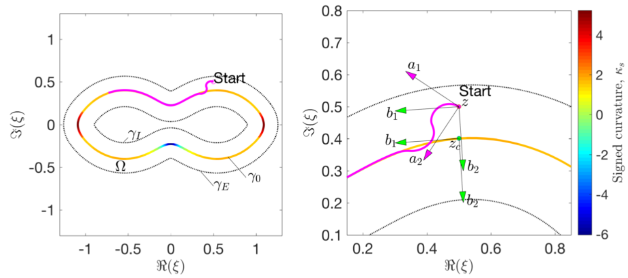

(a) (b)

Fig. 4. a), b) An example that steers a self-propelled particle in a flow field to a unique, non-convex boundary curve. The outer and inner Bertrand curves γ_E and γ_I defined based on the signed curvature are shown in a); Subfigure b) shows the frames of reference needed along with the unique, nearest point z_c for the initial condition

$0 \le |\lambda| < |\lambda_I|$ and z lies on the Bertrand curve γ_λ. Let $z_c = \gamma_0(s_c)$. From the construction of a Bertrand curve at λ, we insert $z - z_c = i\lambda\gamma_0'(s_c)$ into the left-hand side of (28) to produce

$$\lambda \left\langle \gamma_0'(s_c), i\gamma_0'(s_c) \right\rangle ,$$

which vanishes, satisfying the first-order necessary condition (28). Using (26) reduces the second-order condition (29) to

$$\kappa_{\rm s}(s_c) \left\langle i\gamma_0'(s_c), z - \gamma_0(s_c) \right\rangle < 1 \implies \kappa_{\rm s}(s_c)\lambda < 1. \tag{30}$$

This inequality is trivially satisfied if $\kappa_{\rm s}(s_c) = 0$, $\lambda = 0$, or if $\kappa_{\rm s}(s_c)\lambda < 0$, which occurs if γ_0 turns away from z for increasing s. Consider the case of $\kappa_{\rm s}(s_c)\lambda > 0$, so that γ_0 curves towards z. Placing an upper bound on $\kappa_{\rm s}(s_c)\lambda$ yields

$$\kappa_{\rm s}(s_c)\lambda \le |\kappa_{\rm s}(s_c)||\lambda| < \frac{|\kappa_{\rm s}(s_c)|}{\left|\sup\limits_{\sigma}(\kappa_{\rm s}(\sigma)\chi)\right|}.$$

If $\gamma_0(s_c)$ turns towards z, then $\kappa_{\rm s}(s_c)\chi$ is positive. Hence, the supremum yields a positive value, such that

$$\frac{\kappa_{\rm s}(s_c)\chi}{\sup\limits_{\sigma}(\kappa_{\rm s}(\sigma)\chi)} \le 1,$$

implying $\kappa_{\rm s}(s_c)\lambda < 1$ and satisfying condition (29).

For uniqueness of z_c, note that by (27) and the requirement that γ_0 be regular, γ_λ for each λ such that $0 \le |\lambda| < |\lambda_I|$ does not pass through a center of curvature. Therefore, γ_0 may be continuously deformed without changing topologically (i.e., homotoped) using (22) to γ_λ for any λ in $0 \le |\lambda| < |\lambda_I|$. z lies on only one Bertrand curve γ_λ. By this reasoning, z_c is the nearest point on the curve γ_0 and z_c is unique. □

Within the domain Ω defined by Proposition 2 and under the assumption that (8) is valid (i.e., the vehicle can make forward progress), the control law (11) coupled with the streamline steering strategy in (23)–(27) is guaranteed to converge. We note that it is important that γ_I and γ_E are simple curves since the offsets (27) may yield self-intersections for pathological γ_0 curves (e.g., when γ_0 has segments of opposing orientation with relatively near approaches to each other, γ_I may have a self-intersection). To avoid non-simple bounding curves that may be produced by (27), reduce $|\lambda|$ until (22) results in simple bounding curves. Figure 4a shows the domain Ω in an example problem and illustrates steering to a unique, closed streamline. Figure 4b shows the necessary reference frames for utilizing the steering control (11) for the scalar field (24) created by a Bertrand family of curves emanating from a unique, closed streamline.

D. *Steering to boundaries*

The streamline controller of the previous subsection is only valid with the finite domain of Ω for a given curve γ_0. Outside of Ω, we create an additional steering controller by allowing the co-rotating frame streamfunction ψ_R to serve as the scalar field Φ in Proposition 1. If a vehicle is outside of the valid domains of all boundary curves, we take the streamfunction value of the closest boundary curve as a target Θ^{des} for use in Proposition 1. This control law steers the vehicle towards the boundary. Upon entering the valid domain Ω of a boundary curve, the vehicle steers according to the unique streamline control law. Together, these two control laws work in tandem and constitute our hybrid control strategy.

IV. LAGRANGIAN ADAPTIVE SAMPLING ARCHITECTURE

This section provides a novel architecture for adaptive sampling using a guided Lagrangian sensor for estimation of the flow field by making use of augmented observability-based path planning. This architecture handles uncertainty properly by sharing multiple state estimates and associated covariances between the estimator and the path planner. The multiple estimates are utilized in an expected cost analysis that is used for evaluation of the candidate vehicle paths.

A. *Architecture for guided Lagrangian estimation and control*

Figure 5a presents the proposed architecture for nonlinear/non-Gaussian estimation of a flow field using a guided Lagrangian sensor. The feedback loop in Fig. 5a consists of the true dynamics, such as the ocean currents and vehicle dynamics, measurements of vehicle's position, a nonlinear/non-Gaussian estimator, and the Augmented-Observability Planner with expected cost (A-OP). Given a parametric model of the flow field, a self-propelled vehicle, and prior uncertainty of the vehicle state and the environment's parameters, the A-OP creates a route for guided sampling that minimizes the expected cost in augmented unobservability index. The vehicle steers until the next planning period in an open-loop manner using the control signal u that corresponds to the intended vehicle path. Position measurements of the vehicle are available periodically for GMKF. The GMKF combines the prior uncertainty and the uncertain position measurement into a posterior GMM that incorporates all uncertainty of the vehicle's state and the flow field's parameters. At pre-determined planning times, the A-OP generates multiple flow-field maps from a sparse representation of the posterior PDF, creates candidate control signals, and calculates the expected cost in augmented unobservability index by accounting for the probability of occurrence for each state realization it uses.

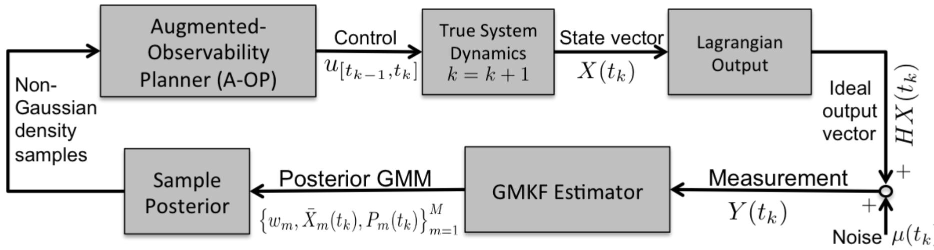

(a)

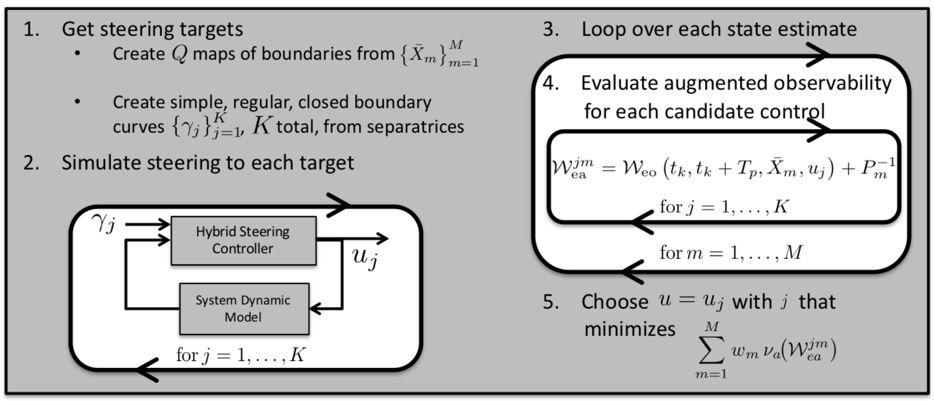

(b)

Fig. 5. a) Overall architecture for estimation and control. b) Algorithmic details of the Augmented-Observability Planner with expected cost.

B. Augmented-Observability Planner with expected cost

The A-OP encapsulates the augmented-observability guidance strategy, which utilizes multiple state estimates with uncertainty for planning. The benefit of using multiple state estimates for planning is demonstrated numerically in Section V-B. A traditional empirical observability analysis requires a state estimate as the initial condition. An augmented-observability analysis calls for a state estimate together with a covariance that quantifies uncertainty in the estimate. The GMKF performs non-Gaussian inference, yielding a non-Gaussian posterior PDF. Extracting an individual statistic from the posterior as an estimate of the state would not fully utilize the PDF. We propose to utilize more of the posterior PDF by extracting multiple state realizations with associated covariances. The AO-P planner combines these multiple state estimates and uncertainties in an expected cost calculation that enables the use of a multimodal PDF for planning.

Choose $D_k = \{y(t_1), y(t_2), \ldots, y(t_k)\}$ to represent a set of measurements accumulated through time index k. Create a sparse approximation of the posterior filtering density

$$p(x|D_k) \approx \sum_{j=1}^{Q} \hat{w}_j \delta(x - x_j) \tag{31}$$

using a sparse sampling of Q points $\{x_j\}_{j=1}^{Q}$ and weights $\hat{w}_j$ chosen such that $\sum_{j=1}^{Q} \hat{w}_j = 1$. For a Monte Carlo sampling of realizations, as Q approaches infinity, (31) converges to the true posterior filtering density [48]. For a small number of representative realizations, the sampling consists of the component modes of a GMM. Indeed, only the means, covariances, and weights are necessary to perfectly recover a GMM approximation of the full PDF. Further, this choice is natural because, by construction of a GMM, each component mode is associated with an accumulation of probability mass.

Given a GMM for the filtering density $p(x|D_k) = \sum_{m=1}^{M} w_m \mathcal{N}(x; \overline{x}_m, P_m)$, one may draw a random sample by selecting component Gaussian m with probability w_m and then sampling from this Gaussian using standard techniques for sampling a multivariate normal distribution (for further details, see [40]). This sampling technique reveals that a GMM may be interpreted as the sum of disjoint probabilities that x is distributed according to Gaussian m. This interpretation motivates choosing $\{\bar{x}_m\}_{m=1}^{M}$ as a sampling of the posterior GMM with weights $\hat{w}_j = w_m$. That is, we choose each Gaussian component with probability w_m and represent each Gaussian by its mean to construct a sparse sampling of the posterior PDF.

For each component mean $\bar{x}_m$, the A-OP finds a flow-field map with corresponding separating boundaries of invariant sets. Using the hybrid controller, the A-OP steers virtual copies of the vehicle to these boundaries to generate candidate control signals. Let $\{u_j\}_{j=1}^{K}$ be the list of candidate control inputs, where K is the total number of candidate signals. Note that the empirical augmented unobservability index $\nu_a(\mathcal{W}_{ea}(t_0, t, x, u_j))$, for a specified control signal u_j, is a random variable that depends on state x, which is stochastic. An approximate expected cost for $\nu_a(\mathcal{W}_{ea}(t_0, t, x, u_j))$ can be calculated using the sparse representation (31) of the PDF, such that

$$\begin{aligned}\mathbb{E}\left[\nu_a(\mathcal{W}_{ea}(t_0, t, x, u_j))\right] &= \int \nu_a(\mathcal{W}_{ea}(t_0, t, x, u_j))p(x)dx \\ &\approx \sum_{m=1}^{M} w_m \nu_a(\mathcal{W}_{ea}(t_0, t, \bar{x}_m, u_j)). \end{aligned} \tag{32}$$

Equation (32) provides the expected augmented unobservability index under control signal u_j. It is a weighted sum of the indices over all considered state realizations. Note that the expected cost involves evaluation of candidate control u_j over realizations $\bar{x}_m$, with $m \neq j$. These cases correspond to implementation of a control that was derived to under a different assumed state. Thus, this calculation takes into account even cases for which the state assumed for planning was incorrect. The A-OP compares the value of (32) across all candidate control inputs and chooses the control signal that minimizes this cost index.

V. Numerical Experiments

This section demonstrates the effectiveness of the proposed adaptive sampling architecture through numerical experiments. First, we describe the setup of the simulations, the initial conditions, and some example runs of the closed-loop system. Second, we present a comprehensive comparison of test cases in which various elements of the architecture (e.g., the non-Gaussian estimator, the adaptive flow map refinement, the augmented observability-based path planning, and the expected cost calculation) are incrementally activated.

A. Simulation setup and closed-loop examples

We study the two-vortex system with unequal vortex strengths. The vortices co-rotate about a fixed location known as the center of vorticity z_{cv}. The vortex strengths and positions are initially unknown and are estimated. We fix

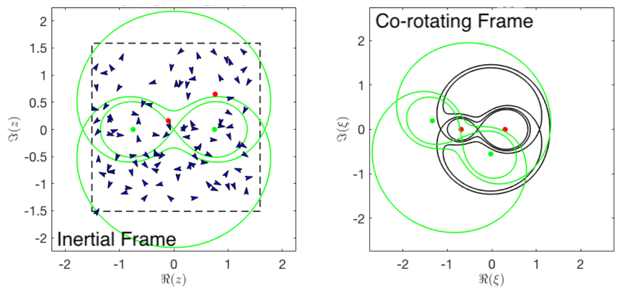

(a) (b)

Fig. 6. a) Initial conditions of the numerical experiments in the inertial frame; initial vehicle locations and orientations are shown as arrow heads; one initial estimate of the vortex locations and their separatrices is shown in green. The true vortices are shown in red. b) The location of the true separatrices are shown in black in the co-rotating frame.

the simulation duration, measurement sampling frequency, time constants associated with planning, controller and estimator gains, initial estimate of the system state, and parameters of the vortices and the vehicle. (Section SM4 of the Supplemental Materials document describes the parameter selection and some representative dimensional quantities.) Large uncertainty in the estimate of the initial condition, which includes vortex circulation strength and position, is used. This choice shows that the GMKF performs well at estimating the state of the system for the two-vortex system from an uncertain initial condition.

The GMKF proficiently estimates the state of the system, however, from arbitrary initial conditions, convergence cannot be guaranteed (e.g., if the initial vortex estimates are highly inaccurate or if a drifting vehicle remains in a region of low observability). To show the robust performance of the proposed architecture, we perform Monte Carlo simulations from random initial conditions broadly covering the sample space of initial conditions. The vehicle launch location and the phase of vortex rotation relative to the vehicle initial position are varied. We sample 100 vehicle positions according to a uniform distribution over a 3×3 nondimensional square area, where the side lengths of 3 units are twice the size of the initial estimate of the vortex separation distance, which was 1.5. Additional sample runs did not noticeably alter the statistics of the run averages beyond 100 samples. Both the true initial phase of rotation for the vortices and the vehicle initial orientation are sampled from the interval $[0, 2\pi]$ uniformly. Figure 6a presents the sampled initial vehicle orientations and locations for the simulations. Figure 6a also illustrates the uncertain initial estimates of the vortex locations along with their separatrices in green. Figure 6b depicts the initial locations of vortices and separatrices in the co-rotating frame of the true vortices at a rotation rate of ω.

Figure 7 shows representative results for three test cases from the same initial condition drawn from those in Fig. 6a. The left three subfigures (Figs. 7a, 7c, and 7e) are in the inertial frame and show Lagrangian measurements used for estimation. The right three subfigures (Figs. 7b, 7d, and 7f) are in the co-rotating frame of the true vortices at a rotation rate of $\omega = 2\pi$ radians/time unit (corresponding to approximately five revolutions during the five time-unit simulation, which represents a one-month deployment). In the first example (Figs. 7a and 7b), a drifting vehicle is launched, tracing out a near-circular trajectory in the inertial frame and remaining on a closed streamline in the outermost invariant set of the co-rotating frame. The trajectory of this drifting vehicle does not provide much insight

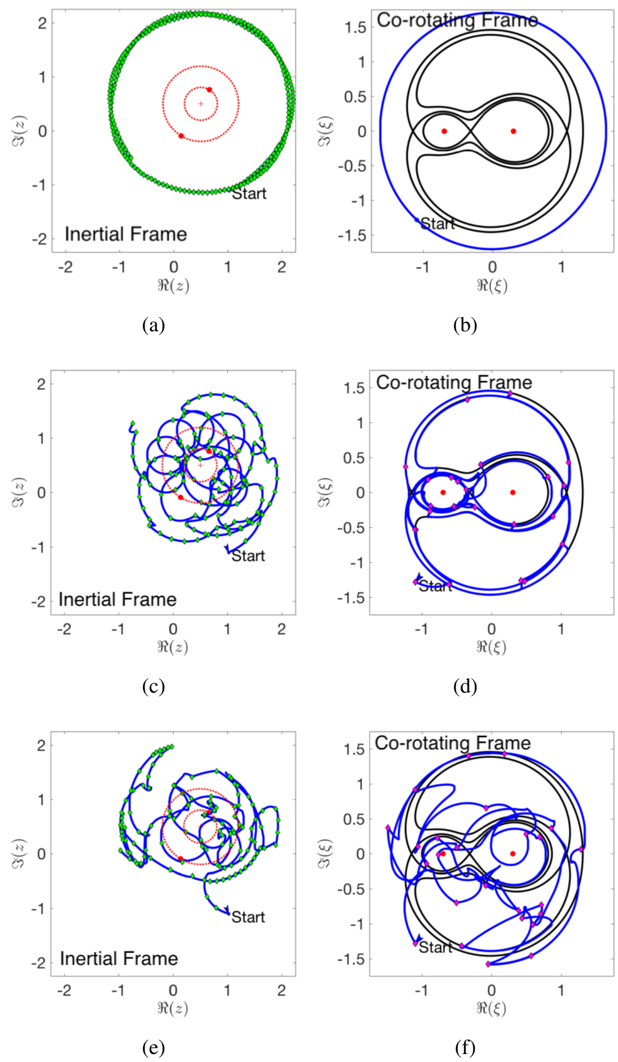

Fig. 7. a and b) Simulation of a drifting vehicle over time interval $[0, 5]$. c, d) Simulation of an observability-guided vehicle with a known flow map over time interval $[0, 2.5]$ (shortened for clarity). e, f) Simulation of an observability-guided vehicle in an estimated flow, navigating according to the A-OP over time interval $[0, 2.5]$ (shortened for clarity). Green diamonds are measurement markers; magenta diamonds are planning markers; red lines trace the path histories of the vortices

in terms of its Lagrangian measurements into the vortex parameters, because many other vortex-pair realizations would yield the same path for the vehicle. In the second example (Figs. 7c and 7d), a self-propelled vehicle with a planner that knows the true flow-field navigates along boundary paths to minimize the unobservability index. Only the first half of the simulation is shown for clarity. In the co-rotating frame, the trajectory explores the separating boundaries of invariant sets, without a priori specification of navigation targets, improving upon previous work [17], which requires a user-specified tour. The exploration of invariant sets in the co-rotating frame produces spirographic trajectory segments in the inertial frame. The inertial trajectory also contains jagged transitions between trajectory segments that correspond to the vehicle changing course at planning times to follow a more observable path.

Figures 7e and 7f present the results of the full closed-loop, guided-Lagrangian sampling architecture. Only the

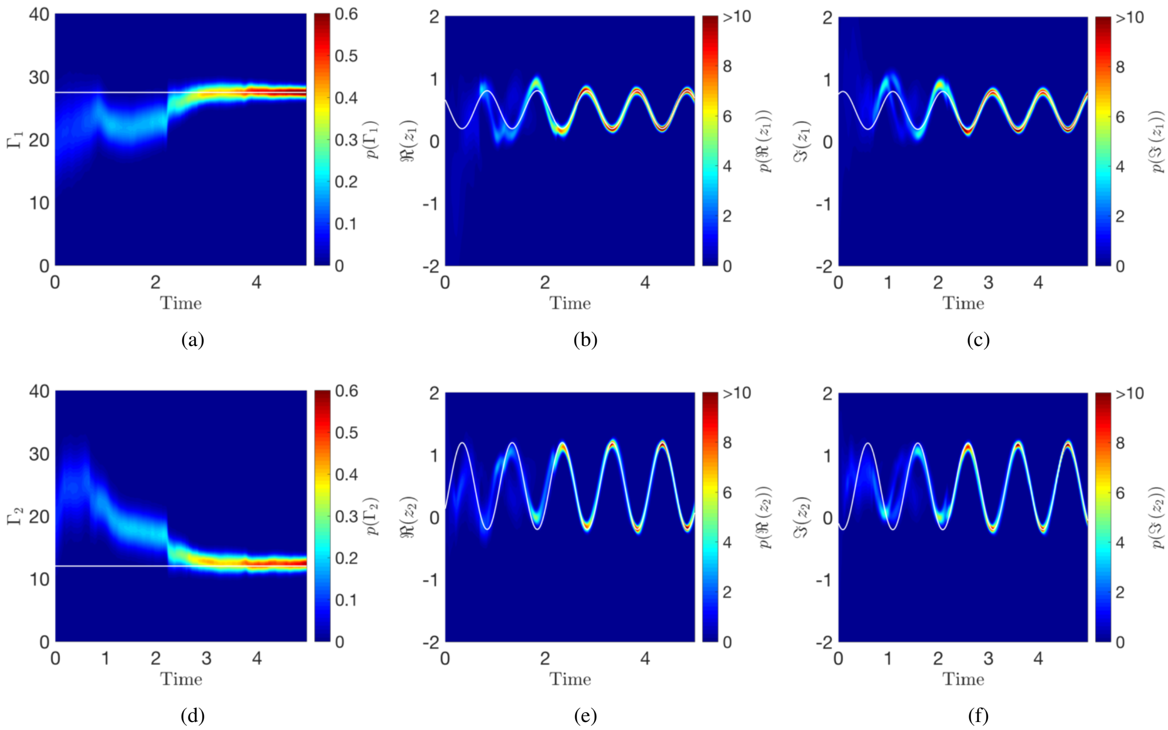

Fig. 8. Estimation results for the closed-loop sampling framework. a)–f) Time histories of the marginalized PDFs for the vortex states

first half of the simulation is shown for clarity. The true flow field is not known to either the estimator or the planner; the vehicle plans using flow-field maps that are adapted using feedback of the guided-Lagrangian measurements. In the co-rotating frame, the vehicle does not clearly navigate along separating boundaries. However, if viewed in the co-rotating frame of the instantaneous state estimate, each trajectory segment in fact steers toward a target separatrix; the overall trajectory is an aggregation of the choices in navigation made by the vehicle to minimize the expected cost in the augmented unobservability index. Later in the simulation, the state estimate improves and the vehicle more closely follows the true flow-field separatrices as shown in Fig. 7d.

During the simulation of the full closed-loop system shown in Figs. 7e and 7f, the vehicle performed GMKF estimation. One to ten Gaussians were adaptively selected by the GMKF to represent the forecast PDF prior to assimilation of data at each measurement time. Figure 8 presents the time histories of marginal PDFs for the vortex strengths and states. The white lines represent the true parameter and state values during simulation. These results show that the closed-loop system can take incorrect initial estimates with large uncertainty and effectively identify and track the two unequal-strength vortices. Although in Figs. 8a and 8d the marginal PDFs for vortex strength are near Gaussian at each time instant, Figs. 8b–8f clearly contain non-Gaussian marginal PDFs for the components of the vortex locations, highlighting the need for a non-Gaussian filter in the architecture.

In multiple simulation runs, the GMKF converged to estimates in which the estimated trajectory of Vortex 1 matched the true trajectory of Vortex 2, and vice versa. Note that the system dynamics are invariant to an interchange of the labels of the vortices, so this condition is benign. The estimator automatically chooses a vortex

TABLE I

MATRIX OF NUMERICAL EXPERIMENTS. IN CASE 8, THE FLOW FIELD IS KNOWN BY THE PLANNER BUT NOT BY THE ESTIMATOR.

Cases	Planning & Control						Estimation		Results
	Off	On					EnKF	GMKF	Estimation error averaged over 100 trials $\sum_k \lVert \bar{x}(t_k) - x^{\text{true}}(t_k) \rVert_2$ (non-dimensional, $\times 10^3$, normalized by Case 8)
		Non-Adaptive	Adaptive						
		Single Est.	Single Est.		Expected Cost				
		Fwd. Obs.	Fwd. Obs.	Aug. Obs.	Fwd. Obs.	Aug. Obs.			
1	X						X		2.95
2	X							X	1.52
3		X						X	1.49
4			X					X	1.31
5				X				X	1.26
6					X			X	1.03
7						X		X	1.02
8		X						X	1.00

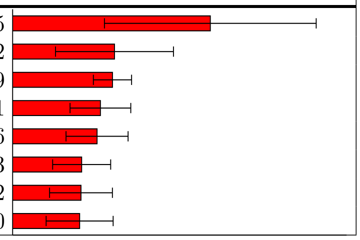

labeling convention within each run. Prior to accumulation of the test results in Table I, we adjust vortex labels to best match the results of the estimator.

B. Test of component-wise performance benefits

To test the performance benefits of each feature of the guided Lagrangian architecture, we considered the eight cases listed in Table I. The check boxes in Table I indicate the subcomponents of the framework that are active in each case. From the 100 randomized initial conditions in Fig. 6a, we execute 100 Monte Carlo runs for each case. Table I also presents a bar graph of the results in terms of estimation error, averaged over all runs for each case. The error bars show one standard deviation from the mean.

Case 1 is a drifting vehicle performing estimation with an Ensemble Kalman Filter (EnKF), which is equivalent to the GMKF with only one Gaussian permitted during the measurement assimilation step. This case is similar to experiments that have been performed in the field (e.g., see [18]). Case 2 is a drifting vehicle with a GMKF for estimation. The gain in estimation performance obtained by use of the GMKF is captured by comparing Case 2 to Case 1, showing a large reduction in estimation error. We note that for many individual runs in Case 1, the estimator failed to properly identify the vortex parameters, leading to poor subsequent tracking. Other variants of the EnKF algorithm exist including features such as covariance inflation and localization [49] that could improve performance. However, we choose a basic EnKF for direct comparison to the GMKF; the algorithms differ only by the number of Gaussians permitted in fitting the forecast PDF.

Cases 3–7 implement guided-Lagrangian sampling using an estimated flow-field map. Case 3 is a self-propelled vehicle guided by an observability-based planner. The candidate controls are generated using the initial flow map that derived from the initial estimate of the flow field, without updating at later times (i.e., the vehicle does not recursively improve its map with new estimates). Case 3 highlights the need for self propulsion in flow-field estimation, because this case performs better than Case 2, in which the vehicle drifts. Case 3 steers the vehicle towards separating boundaries of invariant sets in its non-adapted flow-field map. Since the initial estimate of the flow field is incorrect, the trajectories may correspond to less observable paths with respect to the true flow field. Note that the variance in estimation results is the smallest for Case 3, which is attributable to the use of a non-adapted flow-field map.

Cases 4–7 show that allowing the vehicle to adaptively navigate leads to better flow-field estimation. Similar to Case 3, Case 4 plans its sampling with a forward-looking observability analysis. However, Case 4 uses the mean estimate of the posterior PDF to re-calculate its flow map after assimilation of new data. The estimation error for Case 4 is greatly reduced relative to Case 3, highlighting the need for a self-propelled vehicle to be appropriately guided. Case 5 also adapts the flow map used in planning. However, it also utilizes augmented observability analysis in planning, based upon the overall mean and overall covariance of the posterior distribution. For the set of parameters used in the two-vortex system, Case 5 performs better than Case 4, which only plans sampling based upon a forward-looking observability calculation. Non-Gaussian estimation leads to multi-modal posterior distributions, but note that Cases 3-5 only make use of one or two statistics extracted from the PDF. Extraction of a single statistic for use is consistent with traditional certainty equivalence control (i.e., using a single state estimate for feedback), but it discards much of the information present in a multimodal PDF.

An expected cost calculation allows the path planner to make use of a multimodal PDF by leveraging the GMM representation. Case 6 utilizes the GMM for planning by taking the component modes and creating a possible flow map for each mode. The hybrid steering controller generates candidate trajectories by simulating steering to the separatrices in each of these maps. Case 6 then computes an expected cost in unobservability index for a forward-looking observability analysis for each candidate input. Case 6 demonstrates the benefit of an expected cost calculation, over Cases 4 and 5, in which only single estimates are used for planning. Lastly, Case 7 represents the full architecture for path planning based on augmented-observability and expected cost. Case 7 uses multiple state estimates in an expected cost calculation of augmented unobservability index, in contrast to Case 6, which uses only the unobservability index. Case 7 modestly improves the estimation error relative to Case 6. The improvement from Case 6 to Case 7 is present, but not as prominent as the improvement from Case 4 to Case 5. This effect may be attributed to the use of multiple samples from the posterior PDF Case 6, which effectively encodes some prior information from the PDF without the use of covariance matrices.

Case 8 is a benchmark case in which planning is performed in an ideal manner, but estimation is left up to the GMKF. In Case 8, the planner knows the true flow field, but the truth is hidden from the estimator. A vehicle in this case therefore knows the most observable areas for sampling. As expected, this benchmark case yields the smallest estimation error. Note that the cumulative performance gains for the adaptive sampling architecture cause the average estimation error of Case 7 to closely approach the estimation error under ideal path planning in Case 8.

VI. CONCLUSION

This paper puts forward an architecture for flow-field estimation using a guided Lagrangian sensor. In this framework, a self-propelled Lagrangian sensor is guided along highly observable paths, which we have shown correspond to the separating boundaries of invariant sets. The main elements of the architecture are the hybrid steering controller, the Gaussian Mixture Kalman Filter, and the Augmented-Observability Planner with expected cost. The hybrid steering controller includes a streamfunction-value control law and streamline control law. The streamfunction-value control law steers the vehicle to within a region for which the streamline control law is guaranteed to converge. The streamline control law combines a flow-relative transformation, a Bertrand family of curves, and a steering control law for steering to a unique, closed streamline. The region of validity for the streamline controller is established analytically. The Gaussian Mixture Kalman Filter is a nonlinear/non-Gaussian estimator that produces a non-Gaussian posterior distribution encoding all uncertainty of the state in the form of a Gaussian mixture representation. Using the Gaussian mixture model of the posterior probability density, the Augmented-Observability Planner with expected cost samples the mixture's component means as possible realizations of the state and takes their associated covariances as the uncertainties for these realizations. For each possible realization of the state, the Augmented-Observability Planner with expected cost generates an estimate of the flow field and simulates the vehicle virtually steering to the most informative regions in the flow field. These simulations generate a family of candidate control signals based on the use of the hybrid steering controller. For each candidate control signal, the Augmented-Observability Planner with expected cost calculates the augmented unobservability index, which measures how well the forward-looking observability for the path complements the prior error covariance of the state. This operation is performed for all candidate control signals and all state realizations considered. The Augmented-Observability Planner with expected cost then finds an expected cost for each control signal by taking a weighted sum of the augmented unobservability indices and selects the control signal that minimizes this cost. The resulting control signal is most likely to lead to an informative vehicle trajectory given the prior information and all other state realizations considered. Numerical experiments show the benefit of each component of this architecture on a case study of a two-vortex system, a model that is relevant to the study of ocean eddy dynamics [23], [24], [27].

Extensions of this work should consider more complex flow environments, time-varying flows, and flows for which a parameterized model is not known in advance. Additionally, the inclusion of multiple, cooperative sampling agents will add to the utility of the sampling framework.

Acknowledgment

We acknowledge the participation of Storm Weiner and Amy Davis supported by the National Science Foundation TREND REU (PHY-1461089) in preliminary versions of this work. We acknowledge helpful discussions on the GMKF with Pierre Lermusiaux and Tapovan Lolla. The authors gratefully acknowledge the supercomputing resources from the University of Maryland that were made available for the Monte Carlo simulations in this paper (http://www.it.umd.edu/hpcc).

References

[1] Belbeoch, M.: Argo: Part of the integrated global observation strategy. http://www.argo.ucsd.edu/. Accessed: 2014-12-15.

[2] Katsumata, K., and Yoshinari, H.: Uncertainties in global mapping of Argo drift data at the parking level. J. Oceanogr., Vol. 66, No. 4, 553–569 (2010). https://doi.org/10.1007/s10872-010-0046-4

[3] Ramp, S., Davis, R., Leonard, N., Shulman, I., Chao, Y., Robinson, A., Marsden, J., Lermusiaux, P., Fratantoni, D., Paduan, J., Chavez, F., Bahr, F., Liang, S., Leslie, W., and Li, Z.: Preparing to predict: The Second Autonomous Ocean Sampling Network (AOSN-II) experiment in the Monterey Bay. Deep Sea Res. Part II Top. Stud. Oceanogr. 56, 68–86 (2009). http://dx.doi.org/10.1016/j.dsr2.2008.08.013

[4] Eakins, B., and Sharman, G.: Volumes of the world's oceans from ETOPO1. http://www.ngdc.noaa.gov/mgg/global/etopo1_ocean_volumes.html (2014). Accessed: 21 December 2014.

[5] Paley, D., Zhang, F., and Leonard, N.: Cooperative control for ocean sampling: The Glider Coordinated Control System. IEEE Trans. Control Sys. Tech., 1–10 (2008). http://dx.doi.org/10.1109/TCST.2007.912238

[6] Smith, R., Schwager, M., Smith, S., Jones, B., Rus, D., and Sukhatme, G.: Persistent ocean monitoring with underwater gliders: Adapting sampling resolution. J. Field Robotics 28, 714–741 (2011). http://dx.doi.org/10.1002/rob.20405

[7] Smith, R., Huynh, V.: Controlling buoyancy-driven profiling floats for applications in ocean observation. J. Oceanic Engineering, Vol. 39, No. 3, 571–586 (2014). https://doi.org/10.1109/JOE.2013.2261895

[8] Cannell, C., and Stilwell, D.: A comparison of two approaches for adaptive sampling of environmental processes using autonomous underwater vehicles. Proc. MTS/IEEE Oceans Conf. Vol. 2, 1514 –1521 (2005). http://dx.doi.org/10.1109/OCEANS.2005.1639970

[9] Mourre, B., and Alvarez, A.: Benefit assessment of glider adaptive sampling in the Ligurian Sea. Deep Sea Res. Part I Ocean. Res. Papers 68, 68–78 (2012). http://dx.doi.org/http://dx.doi.org/10.1016/j.dsr.2012.05.010

[10] Lolla, T., Ueckermann, M., Yigit, K., Haley Jr., P., and Lermusiaux, P.: Path planning in time dependent flow fields using level set methods. Proc. IEEE Int. Conf. Robotics Autom., 166–173 (2012). http://dx.doi.org/10.1109/ICRA.2012.6225364

[11] Subramani, D., Lolla, T., Haley Jr., P., and Lermusiaux, P.: A stochastic optimization method for energy-based path planning, In: Dynamic Data-Driven Environmental Systems Science, Vol. 8964, 347–358, Springer (2015). http://dx.doi.org/10.1007/978-3-319-25138-7_31

[12] Kularatne, D., Bhattacharya, S., and Hsieh, M. A.: Time and Energy Optimal Path Planning in General Flows. Robotics: Sci and Sys. Sept (2016). https://doi.org/10.15607/RSS.2016.XII.047

[13] Hinson, B., Binder, M., and Morgansen, K.: Path planning to optimize observability in a planar uniform flow field. Proc. Amer. Control Conf., 1394–1401, Washington DC, (2013). http://dx.doi.org/10.1109/ACC.2013.6580031

[14] DeVries, L., Majumdar, S., and Paley, D.: Observability-based optimization of coordinated sampling trajectories for recursive estimation of a strong, spatially varying flowfield. J. Intell. Robot. Syst. 70, 527–544 (2012) https://doi.org/10.1007/s10846-012-9718-1

[15] Jazwinski, Andrew H.: Stochastic Processes and Filtering Theory. Dover Publications, Mineola, New York, pp. 231–234 (2007).

[16] Leonard, N., Paley, D., Davis, R., Fratantoni, D., Lekien, F., and Zhang, F.: Coordinated control of an underwater glider fleet in an adaptive ocean sampling field experiment in Monterey Bay. J. Field Robotics 27, 718–740 (2010). http://dx.doi.org/10.1002/rob.20366

[17] Lagor, F., Ide, K., and Paley, D.: Incorporating prior knowledge in observability-based path planning for ocean sampling. Sys. Control Lett., Vol. 97, 169–175, (2016). https://doi.org/10.1016/j.sysconle.2016.09.002

[18] Salman, H., Ide, K., and Jones, C.: Using flow geometry for drifter deployment in Lagrangian data assimilation. Tellus A 60, 321–335 (2008). http://doi.org/10.1111/j.1600-0870.2007.00292.x

[19] Michini, M., Hsieh, M. A., Forgoston, E., Schwartz, I. B.: Robotic tracking of coherent structures in flows. IEEE Trans. Robot., Vol. 30, No. 3, 593–603, (2014). http://doi.org/10.1109/TRO.2013.2295655

[20] Kularatne, D., and Hsieh, M. A.: Tracking attracting manifolds in flows. Auton. Robots, Vol. 41, No. 8, 1575–1588 (2017). http://doi.org/10.1007/s10514-017-9628-y

[21] Michini, M., Hsieh, M. A., Forgoston, E., and Schwartz, I. B.: Experimental validation of robotic manifold tracking in gyre-like flows. Proc. IEEE/RSJ Intl. Conf. Intell. Robots and Sys., 2306-2311, Chicago IL, (2014). http://doi.org/10.1109/IROS.2014.6942874

[22] Krener, A., and Ide, K.: Measures of unobservability. Proc. IEEE Conf. Decis. Control, 6401–6406 (2009). http://dx.doi.org/10.1109/CDC.2009.5400067

[23] Southwick, O. R., Johnson, E. R., and McDonald, N. R.: A point vortex model for the formation of ocean eddies by flow separation. Physics of Fluids, Vol. 27, No. 016604, (2015). http://doi.org/10.1063/1.4906112

[24] Flierl, G.: Isolated eddy models in geophysics. Ann. Rev. Fluid Mech., Vol. 19, 493–530, (1987). https://doi.org/10.1146/annurev.fl.19.010187.002425

[25] Simpson, J. J., and Lynn, R. J.: A mesoscale eddy dipole in the offshore California current. J. Geophysical Res., Vol. 95, No. C8, 9–13, (1990). https://doi.org/10.1029/JC095iC08p13009

[26] de Ruijter, W. P. M., van Aken, H. M., Beier, E. J., Lutjeharms, J. R. E., Matano, R. P., and Schouten, M. W.: Eddies and dipoles around South Madagascar: Formation, pathways and large-scale impact. Deep-Sea Res. I. Vol. 51, 383–400, (2004). http://doi.org/10.1016/j.dsr.2003.10.011

[27] Southwick, O. R., Johnson, E. R., and McDonald, N. R.: A simple model for “sheddies ” - Ocean eddies formed from shed vorticity. J. Phys. Ocean., Vol. 46, 2961–2979, (2016). http://doi.org/10.1175/JPO-D-15-0251.1

[28] Zhang, F., and Leonard, N.: Coordinated patterns of unit speed particles on a closed curve. Sys. Control Lett. 56, 397–407 (2007). http://dx.doi.org/10.1016/j.sysconle.2006.10.027

[29] Paley, D., and Peterson, C.: Stabilization of collective motion in a time-invariant flowfield. J. Guid. Control Dyn. 32, 771–779 (2009). http://dx.doi.org/10.2514/1.40636

[30] Bengtsson, T., Snyder, C., Nychka, D.: Toward a nonlinear ensemble filter for high-dimensional systems. J. of Geophysical Res.: Atmos., Vol. 108, No. D24, 8775 (2003). http://dx.doi.org/10.1029/2002JD002900

[31] Sondergaard, T., and Lermusiaux, P.: Data assimilation with Gaussian mixture models using the dynamically orthogonal field equations. Part I: Theory and scheme. Mon. Weather Rev., Vol. 141, 1737–1760 (2013). http://dx.doi.org/10.1175/MWR-D-11-00295.1

[32] Lagor, F., Davis, A., Ide, K., and Paley, D.: Non-Gaussian estimation of a two-vortex flow using a Lagrangian sensor guided by output feedback control. Proc. Amer. Control Conf., Boston, MA (2016) http://dx.doi.org/10.1109/ACC.2016.7525050

[33] Lagor, F., Ide, K., and Paley, D.: Touring invariant set boundaries of a two-vortex system using streamline control. Proc. IEEE Conf. Decis. Control, Osaka, JP (2015). http://dx.doi.org/10.1109/CDC.2015.7402536

[34] Lagor, F.: Path planning, flow estimation, and dynamic control for underwater vehicles. (Doctoral dissertation). University of Maryland (2017). https://doi.org/10.13016/M2ZG6G75S.

[35] Newton, P.: The N-vortex problem: Analytical techniques. Springer, New York (2001)

[36] DeVries, L., and Paley, D.: Multivehicle control in a strong flowfield with application to hurricane sampling. J. of Guid. Control Dyn. 35, 794–806 (2012). http://dx.doi.org/10.2514/1.55580

[37] Powel, N., and Morgansen, K.: Empirical observability Gramian rank condition for weak observability of nonlinear systems with control. Proc. IEEE Conf. Decis. Control, Osaka, JP, 6342–6348 (2015). http://dx.doi.org/10.1109/CDC.2015.7403218

[38] Chen, R., and Liu, J.: Mixture Kalman filters. J. R. Stat. Soc. B 62, 493–508 (2000). http://dx.doi.org/10.1111/1467-9868.00246

[39] Hoteit, I., Pham, D.-T., Triantafyllou, G., and Korres, G.: A new approximate solution of the optimal nonlinear filter for data assimilation in meteorology and oceanography. Mon. Weather Rev. 136, 317–334 (2008). http://dx.doi.org/10.1175/2007MWR1927.1

[40] Bishop, C.: Pattern recognition and machine learning. Springer, New York (2006)

[41] Carreira-Perpinan, M.: Mode-finding for mixtures of Gaussian distributions. IEEE Trans. on Pattern Analysis and Machine Intelligence 22, 1318–1323 (2000). http://dx.doi.org/10.1109/34.888716

[42] McMahon, J., and Plaku, E.: Mission and motion planning for autonomous underwater vehicles operating in spatially and temporally complex environments. J. Oceanic Engineering, Vol. 41, No. 4, 893–911 (2016). https://doi.org/10.1109/JOE.2015.2503498

[43] Baronov, D., and Baillieul, J.: Decision making for rapid information acquisition in the reconnaissance of random fields. Proc. of IEEE 100, No. 3, 776–801 (2012). http://dx.doi.org/10.1109/JPROC.2011.2174101

[44] Hawick, K., and James, H.: Enumerating circuits and loops in graphs with self-arcs and multiple-arcs. Proc. Int. Conf. Found. Comput. Sci., 14–20, Las Vegas (2008).

[45] Zhang, F., and Leonard, N.: Cooperative filters and control for cooperative exploration. IEEE Trans. Autom. Control 55, 650–663 (2010). http://dx.doi.org/10.1109/TAC.2009.2039240

[46] Zhang, F., Justh, E., and Krishnaprasad, P. S.: Boundary tracking and obstacle avoidance using gyroscopic control. In: Johann, A. E. A. (ed.), Recent Trends Dyn. Syst., Vol. 35, Ch.16. 417–445, Springer Basel (2013). http://dx.doi.org/10.1007/978-3-0348-0451-6

[47] Pressley, A.: How much does a curve curve? Elementary differential geometry, Vol. XII, ch. 2, 29–54. Springer, 2nd ed. (2010). http://dx.doi.org/10.1007/978-1-84882-891-9

[48] Arulampalam, M., Maskell, S., Gordon, N., and Clapp, T.: A tutorial on particle filters for online nonlinear/non-Gaussian Bayesian tracking. IEEE Trans. Signal Proc. 50, 174–188 (2002). http://dx.doi.org/10.1109/78.978374

[49] Whitaker, J., and Hamill, T.: Ensemble data assimilation without perturbed observations. Mon. Weather Rev. 130, 1913–1924 (2002). http://dx.doi.org/10.1175/1520-0493(2002)130⟨1913:EDAWPO⟩2.0.CO;2

Francis Lagor is an Assistant Professor in the Department of Mechanical and Aerospace Engineering at the University at Buffalo, The State University of New York. Lagor received his Ph.D. in Aerospace Engineering with an emphasis on Dynamics and Control from the University of Maryland in 2017. Prior to attending the University of Maryland, he worked for Lockheed Martin Space Systems Company. He received an M.S. in Mechanical Engineering and Applied Mechanics from the University of Pennsylvania in 2009 and a B.S. in Mechanical Engineering from Villanova University in 2006. Lagor's research interests focus on estimation, navigation, and control of autonomous systems in complex flow environments.

Kayo Ide is an Associate Professor with joint appointment in the Department of Atmospheric and Oceanic Science, the Center for Scientific and Mathematical Modeling, the Earth System Sciences Interdisciplinary Center, and the Institute of Physical Science and Technology at University of Maryland, where she teaches geophysical dynamics, applied mathematics, scientific computation, and data assimilation. She also leads an interdisciplinary scientific prediction group and collaborates with scientists and practitioners at the Navy, NASA, and NOAA laboratories. Ide received a B.S. degree in Aeronautics from Nagoya University, Japan, and M.S. and Ph.D. degrees in Aeronautics from the California Institute of Technology.

Derek Paley is the Willis H. Young Jr. Professor of Aerospace Engineering Education in the Department of Aerospace Engineering and the Institute for Systems Research at the University of Maryland. Paley received the B.S. degree in Applied Physics from Yale University in 1997 and the Ph.D. degree in Mechanical and Aerospace Engineering from Princeton University in 2007. He teaches introductory dynamics, advanced dynamics, aircraft flight dynamics and control, and nonlinear control. Paley's research interests are in the area of dynamics and control, including cooperative control of autonomous vehicles, adaptive sampling with mobile networks, and spatial modeling of biological groups. Paley is Associate Fellow of the American Institute of Aeronautics and Astronautics and Senior Member of the Institute of Electrical and Electronics Engineers.